ChemComm

COMMUNICATION

View Article Online
View Journal | View Issue

Cite this: *Chem. Commun.*, 2023, 59, 9203

Received 13th June 2023,
Accepted 3rd July 2023

DOI: 10.1039/d3cc02751a

rsc.li/chemcomm

Cycle-dependent morphology and surface potential of germanium nanowire anode electrodes†

Srikanth Kolagatla, [ab] Gearoid A. Collins, [c] Jason I. Kilpatrick, [ab] Emrullah Kargin, [ab] Kevin M. Ryan [c] and Brian J. Rodriguez *[ab]

Germanium nanowire (GeNW) electrodes have shown great promise as high-power, fast-charging alternatives to silicon-based electrodes, owing to their vastly improved Li ion diffusion, electron mobility and ionic conductivity. Formation of the solid electrolyte interphase (SEI) on the anode surface is critical to electrode performance and stability but is not completely understood for NW anodes. Here, a systematic study characterizing pristine and cycled GeNWs in charged and discharged states with SEI layer present and removed is performed using Kelvin probe force microscopy in air. Correlating changes in the morphology of the GeNW anodes with contact potential difference mapping at different cycles provides insight into SEI layer formation and growth, and the effect of the SEI on battery performance.

Identifying ideal anode and cathode electrodes for lithium-ion batteries (LIBs) is crucial given their widespread use in portable electronic devices, electric vehicles, and energy storage systems due to their high energy density and long cycle life.[1–5] The compatibility of an electrochemical system is governed by the cell voltage, which is determined based on the anode, cathode, and electrolyte. In particular, the difference in chemical potential between the anode (μ_A) and the cathode (μ_C) is termed as the working voltage, also known as the open circuit voltage, $V_{OC} = ((\mu_A) - (\mu_C))/e$, where e is the magnitude of an electronic charge.[5] The choice of electrode materials and thereby the anode and cathode potentials with respect to the lowest unoccupied and highest occupied molecular orbitals of the electrolyte, respectively, dictate whether the electrolyte will be reduced on the anode or oxidized on the cathode to form a passivating solid electrolyte interphase (SEI) film.[6,7]

Studying the compositional change and aging mechanism of anode and cathode electrodes has significant importance as they can give new insight into the aging of LiBs, and SEI layer formation, which could help in addressing the ever-increasing power demands and the need for more durable devices, thereby prolonging the life of LIBs.[8–10] The anode component of current commercial LIBs is typically composed of graphite (theoretical capacity of 372 mA h g^{-1});[11] however, germanium (Ge) and silicon (Si) boast multiples of this capacity due their ability to form lithium-rich alloys.[12] The formation of the lithiated alloys $Li_{15}Ge_4$ (1384 mA h g^{-1}) and $Li_{15}Si_4$ (3579 mA h g^{-1}) leads to considerable expansion of bulk Ge and Si ($>300\%$), which causes mechanical pulverization of the material, ultimately limiting the cycle life of Li-alloying anodes. Ge based materials have received less attention than Si based materials due to their commercial cost, although it has a higher rate of diffusivity of Li at room temperature ($\sim 400\times$) and a greater electrical conductivity ($\sim 10\,000\times$) making it suitable for high power applications.[12–16] Several studies have suggested that nanoscale Ge and Si anodes are more robust than bulk materials in terms of cyclic degradation. Among various kinds of nanomaterials, nanowires (NWs) have demonstrated to be capable of withstanding massive volume changes without mechanical pulverization, benefiting from their unique 1D nanostructure and enabling them to be promising anodes for LIBs.[15] Moreover, electrochemical cycling of these NW anodes enables the formation of a porous mesh-like structure of interconnected NWs that show excellent adhesion to the substrate from which they are grown, thereby avoiding material delamination typically seen in bulk Ge and Si.[17] The challenges involved with NWs include the radial expansion on lithiation and SEI formation at the electrode surface mainly during the first cycle leading to decrease in charge and discharge. Also, 1D NW electrodes are stable over long cycling but progressively lead to disintegration of NWs. The SEI layer aids stability and

[a] *School of Physics, University College Dublin, Belfield, Dublin D04 V1W8, Ireland. E-mail: brian.rodriguez@ucd.ie*
[b] *Conway Institute of Biomolecular and Biomedical Research, University College Dublin, Belfield, Dublin D04 V1W8, Ireland*
[c] *Department of Chemical Sciences & Bernal Institute, University of Limerick, V94 T9PX Limerick, Ireland*

† Electronic supplementary information (ESI) available: Experimental details, analysis, work function calculation. See DOI: https://doi.org/10.1039/d3cc02751a

combined with disintegrated NWs reduces the formation of cracks in SEI layer compared to typical LIB electrodes.[7,12]

The work function of a material, like the electrode potential, is a measure of its chemical oxidation state. Thus, studying work function can help in determining the state and composition change of an electrode in different cycling states. For pure elements, the work function is proportional to their electronegativities.[18] Reduction of a solid material decreases its work function, due to both lowering the Fermi level of the substance and changes in the surface dipole.[19] The electrode potential is equal to the volta potential or contact potential difference (CPD) between a metal and a reference metallic electrode at the point of zero charge.[20] In this aspect, scanning probe microscopy (SPM)-based techniques, including the family of voltage-modulated modes such as electrostatic force microscopy, Kelvin probe force microscopy (KPFM), electrochemical atomic force microscopy, and electrochemical strain microscopy can be used to study the localized information at micro- to nanoscales.[21–28] KPFM is a non-contact method used to map the relative surface potential on a variety of electronic and ionic devices, including LIBs, by measuring the CPD between the conductive AFM tip and the sample surface. CPD is defined as VCPD = $(\phi_{tip} - \phi_{sample})/e$ where ϕ_{tip} and ϕ_{sample} are, respectively, the work functions of the tip and the sample. The work function of the tip can be determined *via* calibration against highly oriented pyrolytic graphite or other suitable calibration samples. With this knowledge, the work function of an unknown sample can be determined. While in the absence of an electrolyte, these AFM techniques do not directly measure the in-operando electrode potential of the sample, they provide an alternative electrochemical representation in the form of CPD and sample work function. The significance of the similarity between V_{OC} and V_{CPD} has been investigated using an NCA ($LiNi_{0.80}Co_{0.15}Al_{0.05}O_2$) electrode where a clear correlation between local surface potential and macroscopic electrochemical potential was demonstrated.[29] Further, KPFM has been applied to LIBs where most of the work has been performed on the cathode electrode such as characterizing $LiCoO_2$ electrodes with different charge/discharge cycles,[30] aged and nonaged $LiFePO_4$ electrodes using an *ex situ* method.[31] Other works include *in situ* KPFM measurements on solid state LIBs that focused on the local behaviour of the cathode electrode and uneven de-lithiation on composite electrodes.[27] KPFM has also been used for *in situ* characterization of surface potential distribution on TiO_2 anode films within solid state thin-film LIBs during reversible Li^+ diffusion induced by electric field.[25] Most of the work to date on anode electrodes has been performed on either thin-film or composite electrodes. One work focused on individual single crystalline Si NWs which acted as a model electrode to study the evolution of SEI film and the electrode volume expansion/contraction during the first discharging/charging cycle is *via in situ* AFM; however, surface potential was not measured.[7,32] A clear understanding of expansion and compression of NWs during cycling and SEI formation using morphological imaging, coupled with electrochemical understanding *via* surface potential mapping, is therefore necessary.

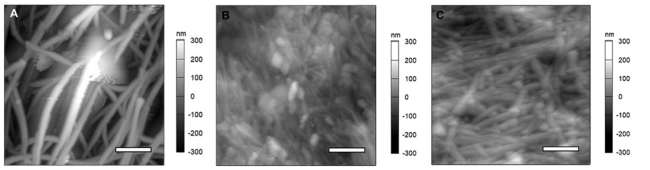

Fig. 1 AFM images of (A) pristine GeNWs, (B) the initial SEI layer formation over GeNWs after 50 cycles, and (C) underlying GeNWs after the removal of the initial SEI layer that formed after the first 50 cycles, respectively. The scale bar in panel A is 600 nm; B and C are 1 μm.

In this work, we systematically characterized the morphological changes of germanium nanowire (GeNW) electrodes from their pristine state to charged and discharged states following 50 and 1500 cycles and correlated these findings with KPFM measurements that mapped the CPD of the charged and discharged electrodes with SEI layer present and removed to show how the surface potential of the electrode changes with cycle time. From this, we reveal how the SEI layer formation affects the charge and discharge capacity in the initial cycle by diffusion of Li^+ ions and further helps retain the capacity over longer cycles by maintaining uniform chemical composition of the electrode.

The AFM topography image of pristine GeNWs on a stainless-steel substrate is shown in Fig. 1(A). The diameters of the pristine GeNWs from the AFM topography image are 130.6 ± 26.9 nm (n = 20 NWs), values likely exaggerated *via* tip broadening. The AFM topography image of cycled GeNWs shown in Fig. 1(B) reveals the surface morphology evolution of the cycled GeNW anode during the first 50 cycles. A rough and inhomogeneous layer of particle-like precipitates, corresponding to the decomposition of electrolyte on the surface, decorates the nanowires. The rough surface and the granular deposits observed on the NWs indicate the growth of SEI layer in initial few cycles, in agreement with literature.[7] The AFM topography image of cycled GeNWs with SEI removed following the first 50 cycles is shown in Fig. 1(C). The AFM image shows that the underlying GeNWs are still intact in the pristine state without any change in the roughness or any granular deposition due to Li ion intercalation. The measured diameter of 143.8 ± 24.3 nm (n = 15) of GeNWs is close to the pristine wires mentioned earlier. This indicates that in the first few cycles only the top layer closest to the electrolyte is participating in the reaction and that the SEI layer growth from the initial cycles reduces the interaction with the underlying GeNWs, which could eventually help in maintaining the electrode charge and discharge capacity over longer cycles.

Further investigation of the degradation of underlying GeNWs after SEI layer removal is undertaken for samples cycled 50 and 1500 times. Fig. 2(A) shows the AFM topography image of GeNWs cycled 50 times, which shows that the GeNWs are still in a pristine state with no granular deposits. The AFM topography image of GeNWs after 1500 cycles, shown in Fig. 2(B) reveals agglomeration of disintegrated GeNWs resulting in the formation of ligaments of active material with an increase in roughness to 200 nm. Such changes in morphology are consistent with SEM-based studies described in literature.[17]

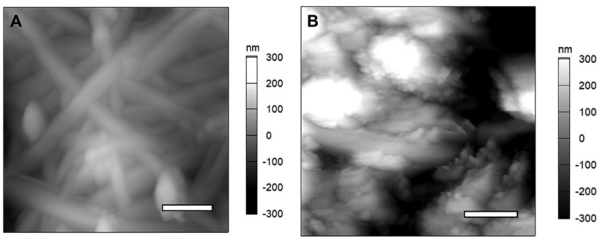

Fig. 2 AFM images of cycled GeNW samples after SEI removal following (A) 50 and (B) 1500 cycles, respectively. The scale bar in panel A is 400 nm; B is 1 μm.

From the topography images after the SEI layer is removed, the GeNWs did not undergo any dramatic morphological changes even after the first 50 cycles. The underlying NWs are still intact with no cracks, supporting the hypothesis that GeNWs have the advantage of withstanding volume changes during the first lithiation/de-lithiation cycles.

At 1500 cycles, all the nanowires are disintegrated to form a porous alloy of Ge combined with lithium and other additives, which is still stable without any evidence of cracks.

GeNW anode electrodes were characterized using KPFM to investigate the change in the CPD over charging and discharging cycles in the presence and absence of the SEI layer. Fig. 3(A) and (B) shows the results for the pristine GeNWs sample. The measured CPD is 627.49 ± 32.04 mV averaged over the whole image. The measured CPD of partial porous GeNWs cycled 50 times and left in the charged state with SEI present is 507.04 ± 15.44 mV (Fig. 3(C) and (D)), whereas the measured CPD of completely porous GeNWs cycled 1500 times and left in the charged state with SEI layer present is 568.29 ± 24.86 mV (Fig. 3(E) and (F)). The CPD is reduced during the initial 50 cycles as the GeNWs become porous. This reduction in the CPD could be due to the partial formation of the SEI layer and the presence of some unreacted GeNWs and could be a reason for the initial drop of charge capacity observed in the first few cycles of charging reported in the literature.[13,15] Subsequently, while the CPD remains lower than that for the pristine case, the CPD increases with complete formation of the SEI layer and fully formed porous GeNW surface with no unreactive GeNWs present in the top surface at the electrolyte interface. This could be the reason for the stable charge capacity observed over the electrode after longer cycling time observed in the literature.[15] The completely formed SEI layer is helping in retaining the continuous ionic movement over the electrode without further decreasing the capacity. From these measurements, the change in measured CPD from the pristine to the cycled state indicates a change in the composition of the electrode due to the presence of a partially formed SEI layer, consistent with a reported charge capacity reduction.[33] As the cycling is continued, the SEI layer is completely formed, and the charge capacity is maintained for longer cycles.[34] It is crucial to maintain the stability of the SEI layer in order for the charge capacity of the electrode to remain stable.

GeNWs electrodes were further studied in a discharged state before and after 50 and 1500 cycles after SEI removal. Fig. 4(A) and (B) shows the AFM topography and CPD images of the pristine GeNW sample at a different location than Fig. 3. The AFM topography images show bundles of stacked GeNWs. The measured CPD over a 1 μm × 1 μm area is 600.92 ± 39.96 mV, a value within the uncertainty reported from Fig. 3(B) data. Fig. 4(C) and (D) shows the AFM topography and CPD images of the GeNWs after 50 cycles. For this sample, the SEI layer formed in the initial 50 cycles was removed, revealing intact GeNWs without any porous structure formation due to cycling in the topography image.

The measured CPD over the 10 μm × 10 μm scan area shows an average CPD of 265.54 ± 9.09 mV, which is lower than the pristine and porous GeNWs measured in the charged state. The lower CPD could be due to the removal of the Li ions from the electrode during the discharge process as well as residual SEI layer and organic additives still present on the electrode. The overall CPD value in the discharge process is more uniform than the charged state, unlike the uneven distribution mentioned in the literature for de-lithiation.[27] The topography and CPD of the GeNWs after 1500 cycles are shown in Fig. 4(E) and (F). The topography image shows the GeNWs completely disintegrated. The porous structure disappeared, and only large

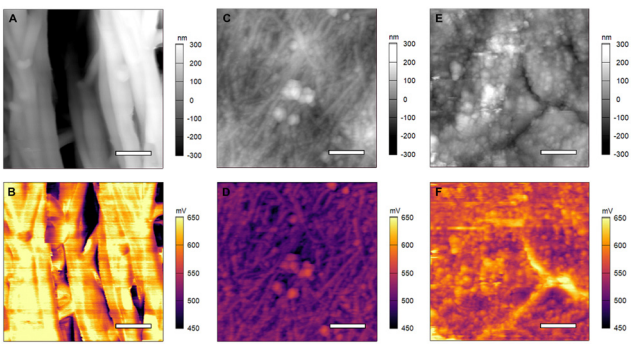

Fig. 3 Topographic and CPD images of (A), (B) pristine GeNWs, (C), (D) partial porous GeNWs with SEI present (50 cycles), and (E), (F) completely porous GeNWs with SEI layer present (1500 cycles). The scale bars in panels A and B are 600 nm; C–F are 1 μm.

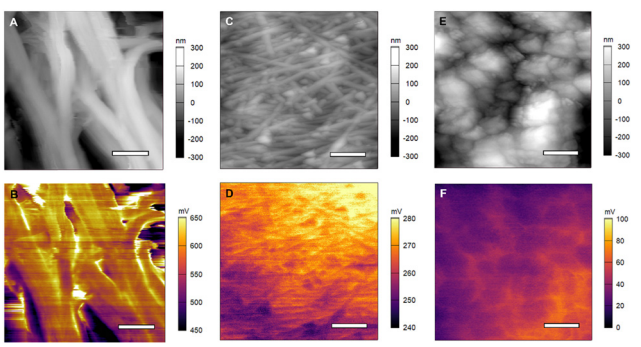

Fig. 4 Topographic and CPD images of (A), (B) pristine GeNWs and cycled and discharged GeNWs after SEI removal following (C), (D) 50 cycles and (E), (F) 1500 cycles. The scale bars in panels A and B are 600 nm; C–F are 1 μm.

agglomerate structures are present. The CPD image shows a measured CPD of 46.68 ± 9.47 mV. The decrease in CPD from pristine and 50 cycles to 1500 cycles suggests unreacted GeNWs are no longer present beneath the agglomerates and there is no possibility for further growth of the SEI layer. The composition of the material on the electrode is indicative of a LiGe composite along with some organic additives, which was reported from bulk measurements in previous studies.[15] From these measurements, the drop in the measured CPD in discharged samples following cycling is indicative of the slow and continuous disintegration of GeNWs during cycling. These results demonstrate that the underlying GeNWs always plays a crucial role in battery performance.

Overall, a similar trend in the measured CPD values from the charged and discharged sample was observed, where the measured CPD decreased with increased cycling, which is also observed in the electrochemical charge and discharge of electrodes shown in a previous publication with similar electrode materials.[15]

In this work, the charging and discharging of GeNWs anode electrodes over 1500 charging cycles was studied using KPFM. The morphology and size of the GeNWs was monitored over 1500 cycles, during which the GeNWs at the surface mechanically disintegrated and formed porous structures. The SEI layer, formed partially in the first 50 cycles, grows into a continuous layer over 1500 cycles.

Characterization of the SEI layer of samples after different numbers of cycles helps understand the role of the SEI in the battery performance. Once the SEI layer is completely formed, it helps retain the battery charge and discharge capacity over longer cycle times. Instability and cracking in the SEI layer could induce a significant material composition change leading to drastic capacity loss and battery failure. Furthermore, this work also shows the importance of KPFM in characterizing the aging effects in battery electrodes. The correlation between surface potential and bulk electrochemical potential could provide new insight into physical and electrical processes, which could help improve the performance and lifetime of Li-ion batteries.

This work was supported by a research grant from Science Foundation Ireland (SFI) and the Sustainable Energy Authority of Ireland (SEAI) under the SFI Career Development Award Grant Number SFI/17/CDA/4637. K. M. R. acknowledges Science Foundation Ireland (SFI) 16/IA/4629 and European Union's Horizon 2020 Research and Innovation Program under grant agreement no. 814464 (Si-DRIVE project). K. M. R. further acknowledges IRCLA/2017/285 and SFI Research Centers MaREI, AMBER, and CONFIRM 12/RC/2278_P2, 12/RC/2302_P2, and 16/RC/3918.

Conflicts of interest

There are no conflicts to declare.

References

1 J. Amici, *et al.*, *Adv. Energy Mater.*, 2022, **12**, 2102785.
2 M. Weiss, R. Ruess, J. Kasnatscheew, Y. Levartovsky, N. R. Levy, P. Minnmann, L. Stolz, T. Waldmann, M. Wohlfahrt-Mehrens, D. Aurbach, M. Winter, Y. Ein-Eli and J. Janek, *Adv. Energy Mater.*, 2021, **11**, 2101126.
3 T. Placke, R. Kloepsch, S. Dühnen and M. Winter, *J. Solid State Electrochem.*, 2017, **21**, 1939–1964.
4 X. Zeng, M. Li, D. Abd El-Hady, W. Alshitari, A. S. Al-Bogami, J. Lu and K. Amine, *Adv. Energy Mater.*, 2019, **9**, 1900161.
5 J. B. Goodenough and K. S. Park, *J. Am. Chem. Soc.*, 2013, **135**, 1167–1176.
6 B. Moeremans, H. W. Cheng, C. Merola, Q. Hu, M. Oezaslan, M. Safari, M. K. van Bael, A. Hardy, M. Valtiner and F. U. Renner, *Adv. Sci.*, 2019, **6**, 1900190.
7 X. R. Liu, X. Deng, R. R. Liu, H. J. Yan, Y. G. Guo, D. Wang and L. J. Wan, *ACS Appl. Mater. Interfaces*, 2014, **6**, 20317–20323.
8 J. P. Pender, G. Jha, D. Hyun Youn, J. M. Ziegler, I. Andoni, E. J. Choi, A. Heller, B. S. Dunn, P. S. Weiss, R. M. Penner and C. Buddie Mullins, *ACS Nano*, 2020, **14**, 51.
9 J. Piątek, S. Afyon, T. M. Budnyak, S. Budnyk, M. H. Sipponen and A. Slabon, *Adv. Energy Mater.*, 2021, **11**, 2003456.
10 Ma Jianmin, *et al.*, *J. Phys. D: Appl. Phys.*, 2021, **54**, 183001.
11 J. Asenbauer, T. Eisenmann, M. Kuenzel, A. Kazzazi, Z. Chen and D. Bresser, *Sustainable Energy Fuels*, 2020, **4**, 5387–5416.
12 T. Kennedy, M. Brandon and K. M. Ryan, *Adv. Mater.*, 2016, **28**, 5696–5704.
13 E. Mullane, T. Kennedy, H. Geaney and K. M. Ryan, *ACS Appl. Mater. Interfaces*, 2014, **6**, 18800–18807.
14 H. Geaney, G. Bree, K. Stokes, G. A. Collins, I. S. Aminu, T. Kennedy and K. M. Ryan, *Chem. Commun.*, 2019, **55**, 7780–7783.
15 G. Flynn, K. Palaniappan, M. Sheehan, T. Kennedy and K. M. Ryan, *Nanotechnology*, 2017, **28**, 255603.
16 H. Geaney, G. Bree, K. Stokes, G. A. Collins, I. S. Aminu, T. Kennedy and K. M. Ryan, *Chem. Commun.*, 2019, **55**, 7780–7783.
17 T. Kennedy, E. Mullane, H. Geaney, M. Osiak, C. O'Dwyer and K. M. Ryan, *Nano Lett.*, 2014, **14**, 716–723.
18 S. Yamamoto, K. Susa and U. Kawabe, *J. Chem. Phys.*, 1974, **60**, 4076.
19 A. Etxebarria, S. L. Koch, O. Bondarchuk, S. Passerini, G. Teobaldi and M. Á. Muñoz-Márquez, *Adv. Energy Mater.*, 2020, **10**, 2000520.
20 V. S. Bagotsky, *Fundamentals of Electrochemistry*, 2nd edn, 2005, pp.1–722.
21 Z. Zhang, S. Said, K. Smith, R. Jervis, C. A. Howard, P. R. Shearing, D. J. L. Brett, T. S. Miller, Z. Zhang, S. Said, K. Smith, R. Jervis, P. R. Shearing, D. J. L. Brett and T. S. Miller, *Adv. Energy Mater.*, 2021, **11**, 2101518.
22 Q. Gao, W.-Y. Tsai and N. Balke, *Electrochem Sci. Adv.*, 2022, **2**, e2100038.
23 N. Balke, S. Jesse, A. N. Morozovska, E. Eliseev, D. W. Chung, Y. Kim, L. Adamczyk, R. E. García, N. Dudney and S. V. Kalinin, *Nat. Nanotechnol.*, 2010, **5**, 749–754.
24 N. Balke, S. Kalnaus, N. J. Dudney, C. Daniel, S. Jesse and S. V. Kalinin, *Nano Lett.*, 2012, **12**(7), 3399–3403.
25 J. Zhu, K. Zeng and L. Lu, *J. Appl. Phys.*, 2012, **111**, 63723.
26 S. Y. Luchkin, H. Y. Amanieu, D. Rosato and A. L. Kholkin, *J. Power Sources*, 2014, **268**, 887–894.
27 H. Masuda, N. Ishida, Y. Ogata, D. Ito and D. Fujita, *Nanoscale*, 2017, **9**, 893–898.
28 S. V. Kalinin, O. Dyck, N. Balke, S. Neumayer, W. Y. Tsai, R. Vasudevan, D. Lingerfelt, M. Ahmadi, M. Ziatdinov, M. T. McDowell and E. Strelcov, *ACS Nano*, 2019, **13**, 9735–9780.
29 X. Zhu, R. I. Revilla and A. Hubin, *J. Phys. Chem. C*, 2018, **122**, 28556–28563.
30 J. Wu, S. Yang, W. Cai, Z. Bi, G. Shang and J. Yao, *Sci. Rep.*, 2017, **7**, 11164.
31 S. C. Nagpure, B. Bhushan and S. S. Babu, *J. Power Sources*, 2011, **196**, 1508–1512.
32 J. Zheng, H. Zheng, R. Wang, L. Ben, W. Lu, L. Chen, L. Chen and H. Li, *Phys. Chem. Chem. Phys.*, 2014, **16**, 13229–13238.
33 S. J. An, J. Li, C. Daniel, D. Mohanty, S. Nagpure and D. L. Wood, *Carbon N. Y.*, 2016, **105**, 52–76.
34 B. Wu, C. Chen, D. L. Danilov, M. Jiang, L. H. J. Raijmakers, R.-A. Eichel and P. H. L. Notten, *ACS Omega*, 2022, **7**, 32740–32748.

